Energetic Electrons Below the Inner Radiation Belt

R. S. Selesnick, Yi-Jiun Su, J. -A. Sauvaud

AGU100 ADVANCING EARTH AND SPACE SCIENCE

JGR Space Physics

RESEARCH ARTICLE
10.1029/2019JA026718

Energetic Electrons Below the Inner Radiation Belt

R. S. Selesnick[1], **Yi-Jiun Su**[1], **and J.-A. Sauvaud**[2]

[1]Space Vehicles Directorate, Air Force Research Laboratory, Kirtland AFB, Albuquerque, NM, USA, [2]Institut de Recherche en Astrophysique et Planétologie, Université de Toulouse, CNRS, UPS, CNES, Toulouse, France

Key Points:
- High-intensity electrons occasionally appear below the inner radiation belt at L < 1.1 with kinetic energy up to 200 keV
- They may be injected from the inner belt by an enhanced convection electric field ~5 mV/m
- Concurrent satellite observations provide high energy resolution and local time coverage during magnetic storms in 2004 and 2006

Correspondence to:
R. S. Selesnick,
richard.selesnick@us.af.mil

Citation:
Selesnick, R. S., Su, Y.-J., & Sauvaud, J.-A. (2019). Energetic electrons below the inner radiation belt. *Journal of Geophysical Research: Space Physics*, *124*, 5421–5440. https://doi.org/10.1029/2019JA026718

Received 11 MAR 2019
Accepted 6 JUN 2019
Accepted article online 13 JUN 2019
Published online 18 JUL 2019

Abstract Energetic electrons have occasionally been observed with high intensity in the low-latitude quasi-trapping region, below the inner radiation belt, where their intensity is normally low. During magnetic storms in November 2004 and July 2006, electrons reached magnetic drift shells with $L < 1.1$. Data from the IDP electron spectrometer on the DEMETER satellite provide high energy resolution, while multiple NOAA/POES satellites provide local time coverage. After accounting for instrumental effects caused by the high intensity, electron kinetic energy is shown to reach at least 200 keV with generally softer spectra than are normally found in the stable trapping region. Electron injection from the inner belt by an enhanced convection electric field ~5 mV/m may explain the observations. This could provide remote testing for models of global electrodynamics.

1. Introduction

Inner radiation belt electrons are stably trapped by the geomagnetic field at altitudes $\lesssim 10^4$ km, with kinetic energies usually $\lesssim 2$ MeV, but their intensity varies as a result of impulsive radial transport caused by fluctuating electric fields and steady losses to atmospheric drag and nuclear scattering (Selesnick, 2016; Selesnick et al., 2016; Su et al., 2016). Scattering by very low frequency (VLF) plasma waves is also significant (Albert et al., 2016; Selesnick et al., 2013), but losses generally are well understood compared to transport because large-scale electric fields have not been accurately characterized.

Satellites in low-altitude orbit $\lesssim 10^3$ km usually observe intense geomagnetically trapped electrons only in the vicinity of the South Atlantic Anomaly (SAA), where particle drift shells reach their lowest altitude. At other locations, they are below the main radiation belt where they typically are exposed only to short-lived radiation of low intensity. These electron may be scattered from the main radiation belt but only on drift shells that extend above a satellite orbit into the stable trapping region. On shells that remain entirely below the main belt, at low geomagnetic latitude, electrons are normally observed with even lower intensity and only as a result of the local neutron-decay source (Zhang et al., 2019).

High electron intensity has been observed intermittently on low-latitude drift shells below the inner belt from electrons of relatively low energy ~40 keV (Suvorova, 2017; Suvorova et al., 2014). Here we describe two examples of related, but less common, low-latitude electron enhancements observed at higher energy during magnetic storms. Their possible implications for the large-scale electric fields that cause radial electron transport are also considered. Data are from particle detectors on the DEMETER satellite (altitude ~700 km, inclination 98°) and the NOAA/POES satellite series (altitude 800–850 km, inclination 98–99°). The low altitude, high inclination orbits are ideal for this study. As is common for inner belt observations, careful attention to details of the detector response characteristics is required for accurate data interpretation. In this regard, it is beneficial to compare data from the different detectors and from events of different magnitude, as will be described.

2. Magnetic Coordinates and Particle Trapping

Electron data will be described in coordinates derived from the IGRF-12 model of the geomagnetic field (Thébault et al., 2015) evaluated at the date of each measurement. This is a degree-13 multipole expansion of the internal field and is used here without any external field model.

Drift shells are labeled by McIlwain L, evaluated for locally mirroring particles with IGRF-12 but using a fixed value for Earth's dipole moment of $k_0 = 0.3\ G R_E^3$ (Roederer, 1970, equation 4.21), which is near the IGRF-12 dipole moment for 2005 of $0.30034\ G R_E^3$ with the Earth radius $R_E = 6,371.2$ km.

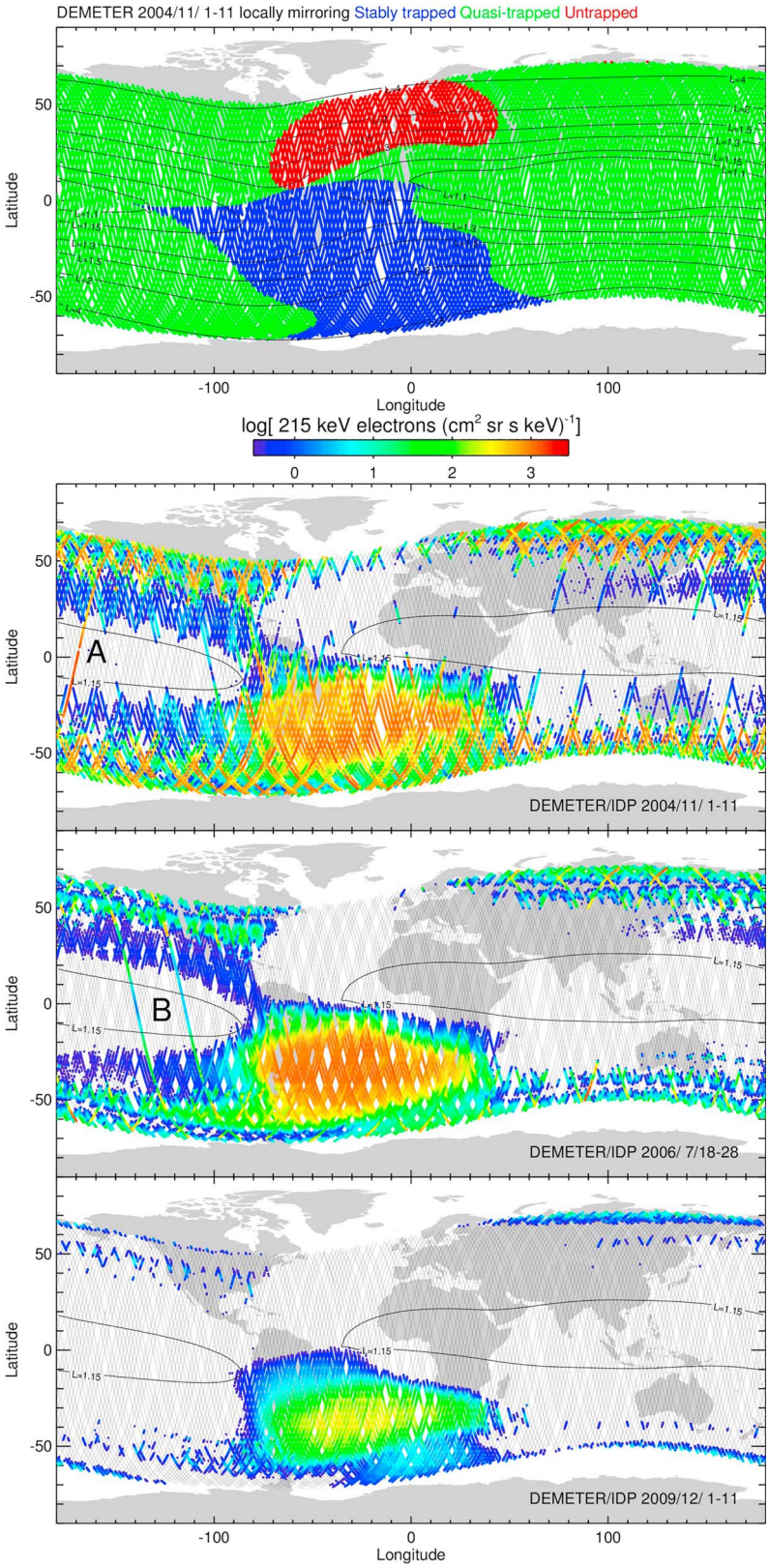

Figure 1. (top) DEMETER orbital tracks over a world map, color coded to show the three trapping regions for locally mirroring particles. Contours of constant L were computed for an altitude of 720 km (from which the satellite altitude differs by roughly ±20 km). (bottom) DEMETER orbital tracks for three selected 11-day intervals, color coded by measured electron intensity. Electron events reaching $L < 1.15$ with high intensity are labeled A and B.

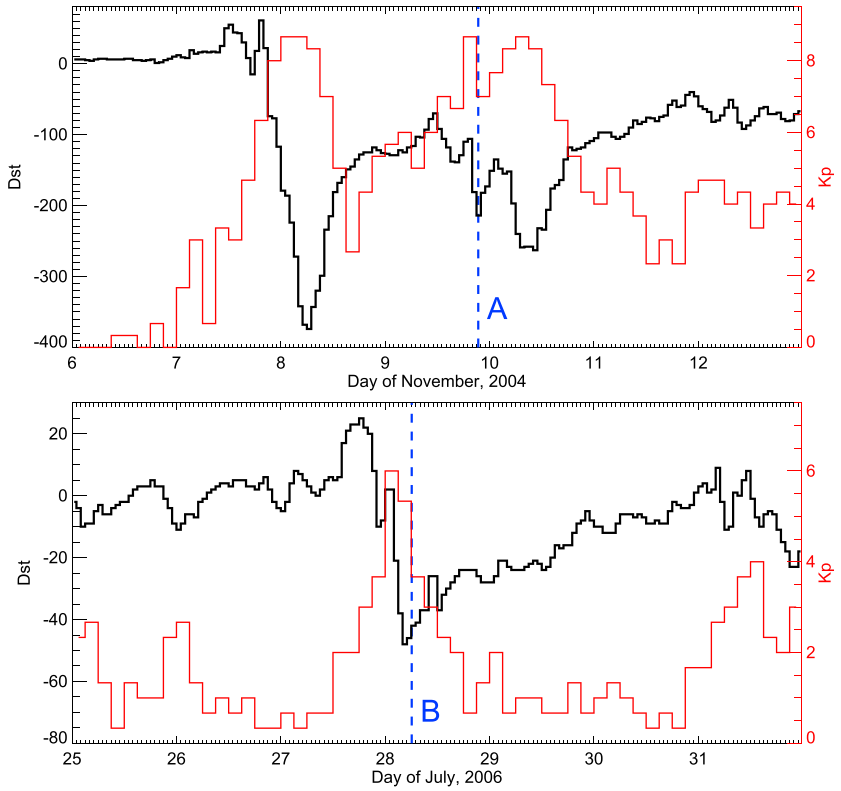

Figure 2. Geomagnetic D_{st} (black) and K_p (red) indices versus time for 7-day intervals in (top) November 2004 and (bottom) July 2006, labeled at the start of each day. Times of the A and B events are indicated (dashed blue).

Trapping conditions for locally mirroring particles are defined by comparing the IGRF-12 local field magnitude B to the minimum north or south field magnitude of the local field line 100-km altitude foot points, B_{100}, and to B'_{100}, the minimum north or south 100-km altitude field magnitudes at any location on an entire drift shell defined by B and L (Selesnick, 2015). Stably trapped particles have $B'_{100} > B$, meaning they never go below 100 km, quasi-trapped have $B_{100} > B > B'_{100}$, meaning they will go below 100 km within one drift, and untrapped have $B > B_{100}$, meaning they will go below 100 km within one bounce.

3. Radiation Maps

The three trapping regions for locally mirroring particles are illustrated by color coding of DEMETER orbital tracks over the upper world map in Figure 1. In the quasi-trapped (green) and untrapped (red) regions, the satellite is below the main radiation belt, which is stably trapped at higher altitude and in the SAA region (blue). Contours of constant L are also shown. The inner belt is typically defined roughly by $L < 2.5$ and the outer belt by $L > 3$, with the slot region in between.

Radiation belt particles are measured on DEMETER by the IDP electron spectrometer (Sauvaud et al., 2006). Intensity measured by IDP, nominally from 215-keV electrons in this case, is shown on the three lower world maps of Figure 1 for separate 11-day intervals, by color coding of orbital tracks. The first two intervals were chosen to include quasi-trapped electron enhancements, labeled A and B, that were observed, respectively, on 9 November 2004 and 28 July 2006 (the B event was observed on consecutive orbits). Both extend to low latitude, with $L < 1.15$, and are well removed from the SAA. Intense quasi-trapped electrons are frequently seen at higher L, as shown in both maps, but rarely at such low L. The third interval is in 2009, when the electron radiation belt had decayed to an unusually low level (Selesnick, 2015), and was chosen to show the extent of the SAA trapped radiation during quiet times. Possible IDP response to radiation belt protons during this and other time periods is considered in Appendix A.

The stable trapping region observable by DEMETER includes $L > 1.1$ (upper map), but stably trapped electrons are normally observed in the SAA only for $L > 1.15$ (lower three maps). This is because scattering

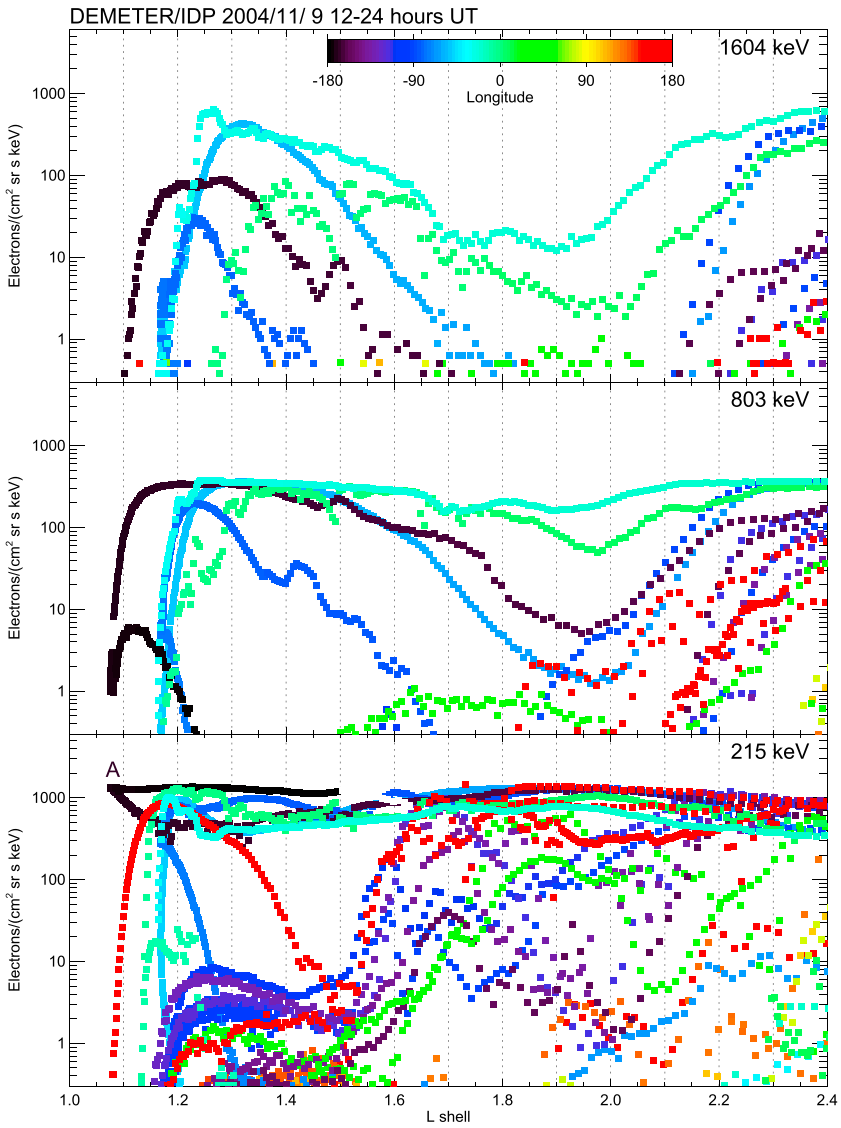

Figure 3. Measured electron intensity versus L, for selected IDP energies, from a 12-hr interval including the A event (labeled at 215 keV as in Figure 1), color coded by geographic longitude.

lifetimes are short, even in the stable trapping region, for $L < 1.15$ (Selesnick, 2012); that is, the 100-km mirror altitude does not define a sharp boundary for electron loss at low L. The $L = 1.15$ contour, included on the intensity maps, demonstrates that the A and B events were observed even at locations below the normal lower L limit of the intense inner electron belt.

4. Geomagnetic Activity

Geomagnetic indices for 7-day intervals centered on 9 November 2004 and 28 July 2006 are shown in Figure 2, including D_{st} (black) and K_p (red). Times of the A and B events from Figure 1 are also indicated (dashed blue). Each event occurred during the recovery phase of a geomagnetic storm, with minimum D_{st} values of (A) −374 nT and (B) −48 nT. They also followed K_p increases to high levels, of (A) 8+ and (B) 6, normally associated with enhanced magnetospheric convection.

The November 2004 magnetic storm was one of the strongest during solar cycle 23 and has been studied extensively. Further details on the geomagnetic and solar wind conditions during that period are readily available (Hui & Vichare, 2019, and references therein).

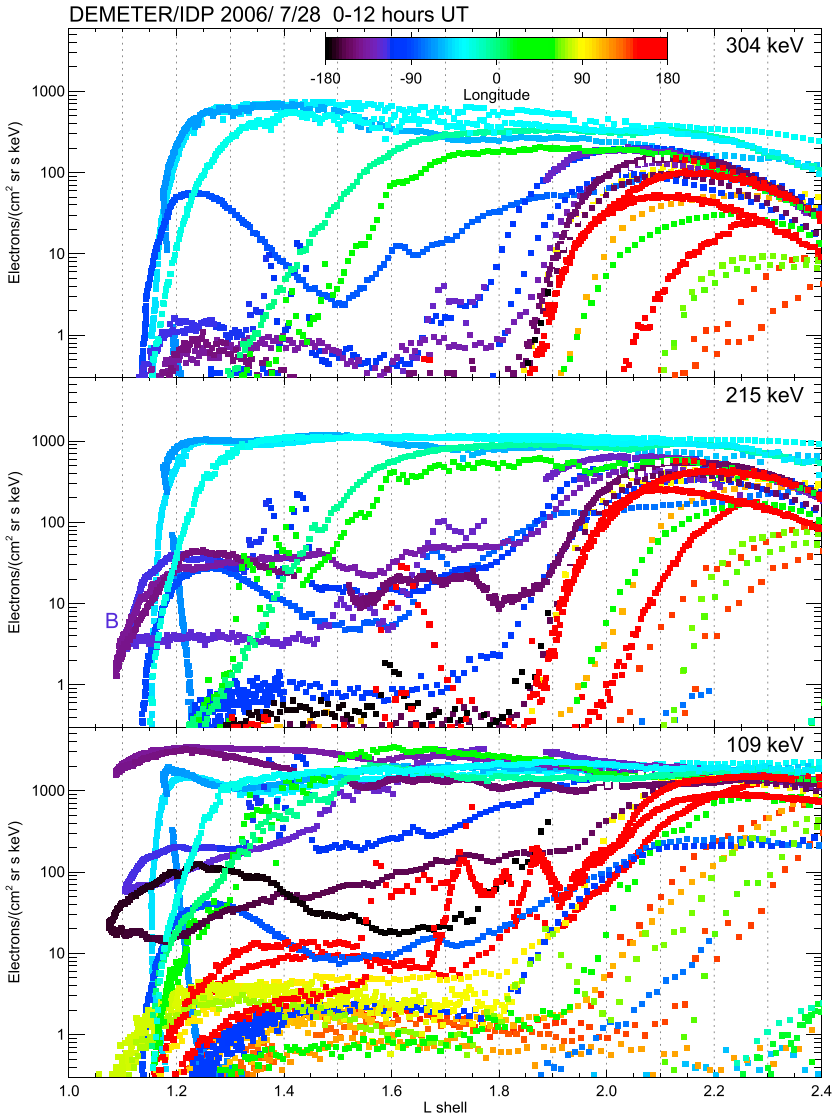

Figure 4. Similar to Figure 3 but for the B event and different selected IDP energies.

5. Radial Intensity Profiles

5.1. DEMETER

Intensity measured by IDP during separate 12-hr (~7 orbit) intervals on 9 November 2004 and 28 July 2006 is shown as a function of L in Figures 3 and 4, respectively. The intervals were chosen to include the labeled A and B events from Figure 1. Data from three channels are shown, selected in each case from the 128 available and labeled by the nominal electron energy. Channel width is 17.8 keV and color coding is by geographic longitude.

In geomagnetically quiet times, significant intensity is seen only during SAA passes (blue and green in the figures) and for $L > 1.15$ (see quiet-time data compared to a quiet inner belt model in Appendix B). For the intervals shown, the A and B events are also seen as significant quasi-trapped intensities reaching $L < 1.1$.

Event A (Figure 3) reaches higher nominal electron energy than event B (Figure 4), but it will be shown that this is largely misleading, due to pulse pileup, and actual energies are usually lower. Measurements are also frequently saturated near 10^3/(cm^2 sr s keV), meaning the true intensity is higher, during some SAA passes and some of the low L events, but the exact saturation level is variable depending on channel and energy spectrum (see Appendix C).

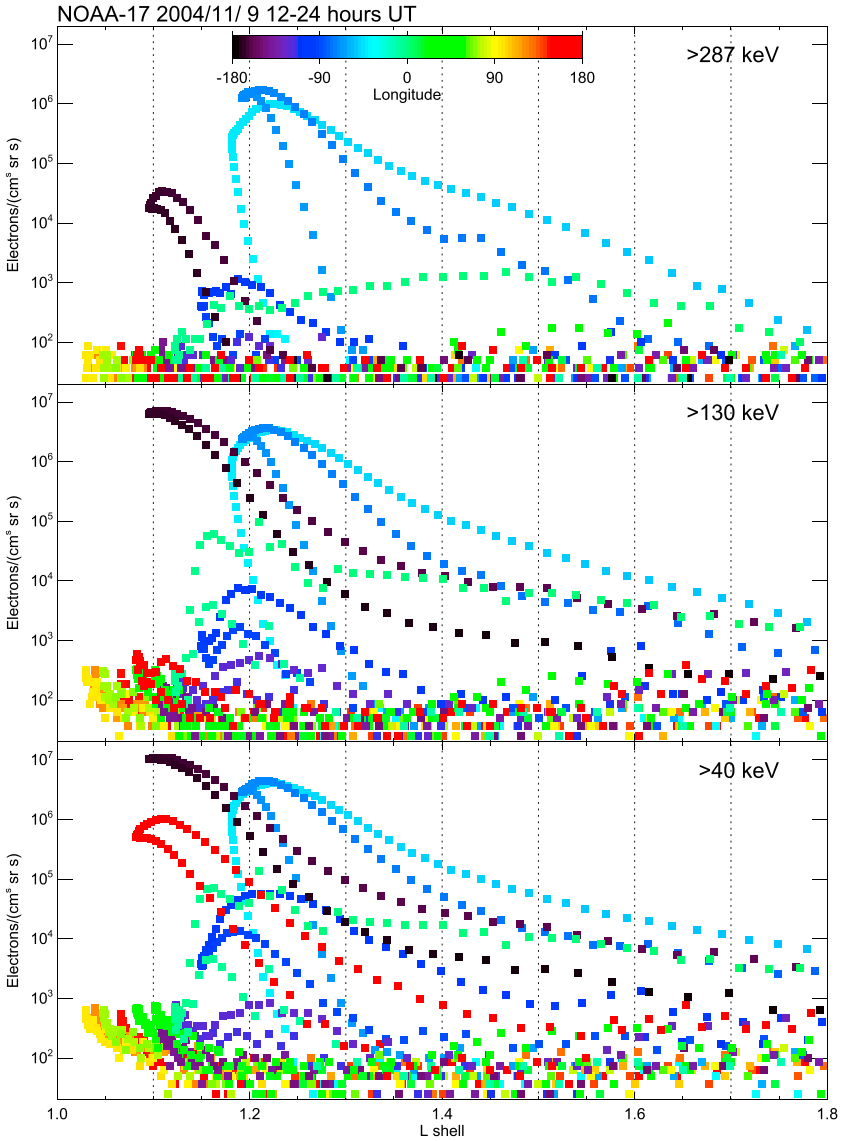

Figure 5. Measured electron integral intensity versus L from the three NOAA-17/MEPED electron channels, for a 12-hr interval including the A event, color coded by geographic longitude.

5.2. POES

The NOAA/POES satellites have similar orbits to DEMETER and provide energetic electron measurements from three integral channels of the MEPED electron telescopes (Evans & Greer, 2000). Only data from the 0-degree telescope are considered here because, at low latitude, it is oriented nearly perpendicular to the local magnetic field (while the 90-degree telescope is nearly parallel, the reverse of their usual arrangement). Intensities will be seen to generally decrease for $L > 1.3$ as the 0-degree telescope becomes more aligned to the local magnetic field.

Intensity versus L during the 12-hr periods of events A and B are shown, respectively, from NOAA-17 in Figure 5 and from NOAA-15 in Figure 6, for comparison to the DEMETER data in Figures 3 and 4. In the POES case there is no apparent saturation and measured intensity reaches significantly higher values relative to DEMETER, even accounting for the integral and differential nature of the two measurements. Most of the high-intensity data are again from SAA passes for $L > 1.15$ (blue and green), but quasi-trapped electrons are again observed to reach $L < 1.1$ (black and red) during the events. In event A (Figure 5) quasi-trapped electrons reach higher intensity than the stably trapped electrons at higher L, but in event B (Figure 6) they are lower and seen only in the two lower energy channels.

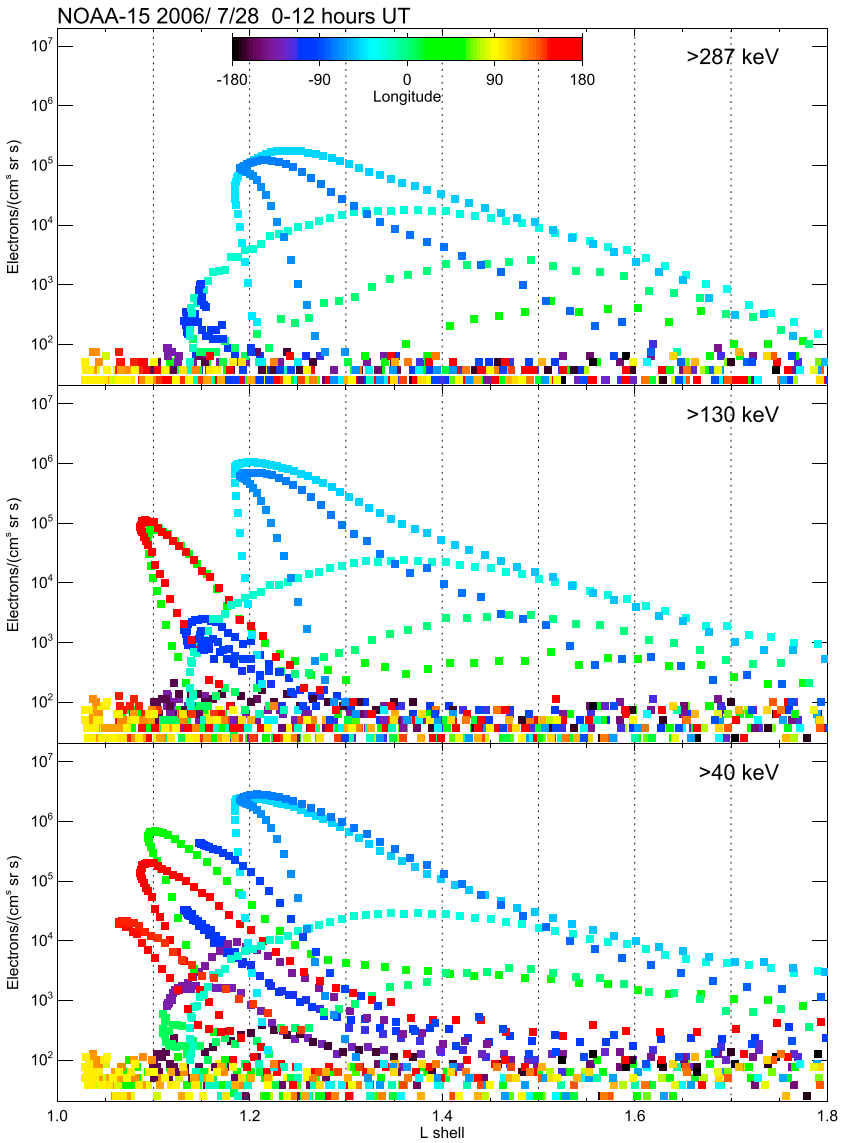

Figure 6. Similar to Figure 5 but for the B event measured on NOAA-15.

6. Energy Spectra

The IDP data provide high-resolution (17.8 keV) electron energy spectra. These are shown at three selected L values, color coded by the UT hour of measurement, for the 12-hr A and B event periods in Figures 7 and 8 respectively (with differing energy scales). Stably trapped electrons (dotted lines) are distinguished from quasi-trapped electrons (solid lines). Both are present at $L = 1.2$ and $L = 1.15$, but only quasi-trapped electrons are present at $L = 1.1$.

For event A (Figure 7) the lowest L electrons were first seen near 21:30 UT and again an orbit later near 23:00 UT, but this time only for the lower energies. However, as already mentioned, the hard spectra that reach above 1 MeV are inaccurate due to pileup.

For event B (Figure 8) the intensities are lower and pileup is not expected for the lower L values. This is supported by some spectral structure even at $L = 1.1$. Electrons were first seen there near 7:00 UT and again an orbit later near 8:30 UT with a softer spectrum. Significant spectral structure, with multiple local minima and maxima, is also seen in the SAA data at low L, as is typically observed during geomagnetically active times (Sauvaud et al., 2006).

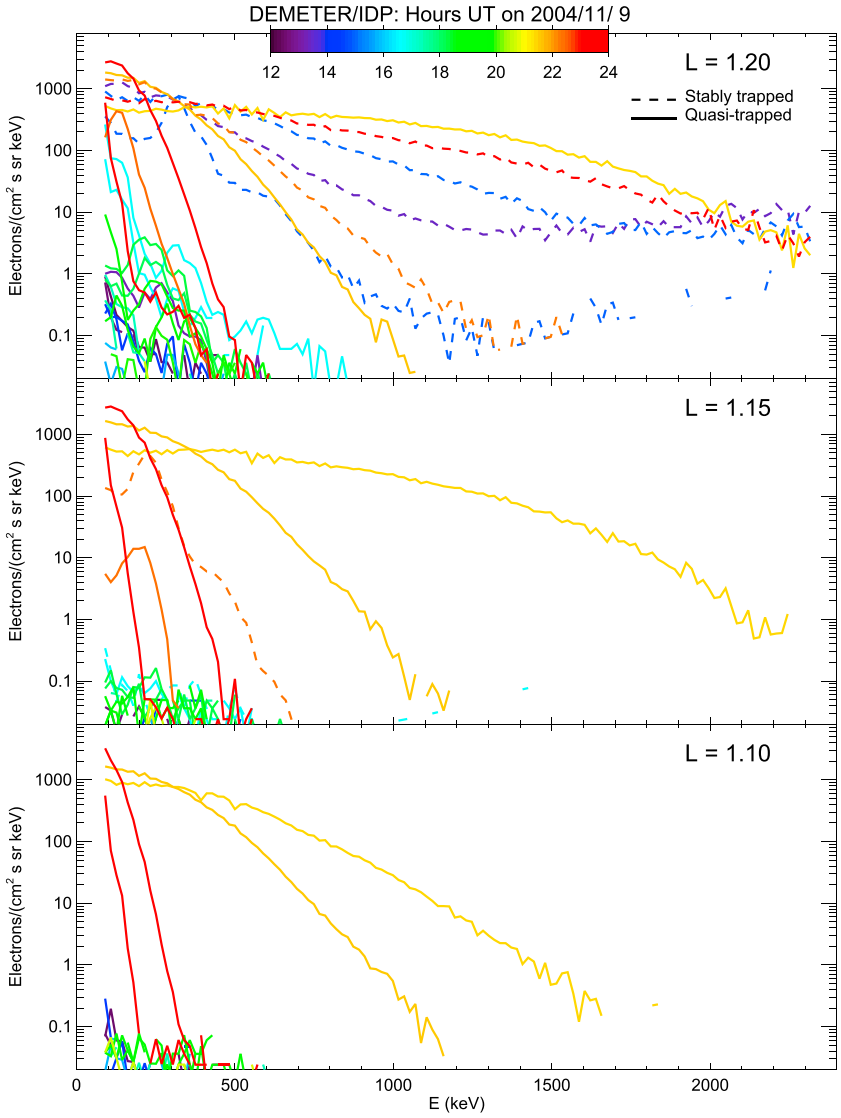

Figure 7. Electron energy spectra during the A event period measured by IDP at selected L and color coded by UT. Data are from regions of quasi-trapping (solid) and stable trapping (dashed).

7. Local Time Dependence

The DEMETER and NOAA-17 satellites both orbited near the 10:00/22:00 local time plane. Other NOAA satellites have different orbital planes, providing evidence of local time dependence in the low L electron data, as shown for the A and B events in Figures 9 and 10, respectively. Orbital tracks for the DEMETER, NOAA-15, and NOAA-16 satellites are represented in polar coordinates, L versus magnetic local time (MLT), for each 12-hr event interval, color coded by measured electron intensity. Data from all trapping regions are included, but only quasi-trapped electrons reach $L < 1.1$ (Figure 1).

The figures show different local time dependences in the low L extent of the two events. The A event reached $L < 1.1$ in the morning sector (Figure 9), as observed by DEMETER, NOAA-15, and NOAA-17 (not shown because of its similar local time to DEMETER). The B event reached $L < 1.1$ in the late afternoon to evening sector (Figure 10), as observed by the same satellites at the opposite phases of their orbits. NOAA-16 did not reach $L < 1.1$ in the afternoon sector for event A or in the post-midnight sector for event B, but electrons were observed with $L < 1.15$ at those local times.

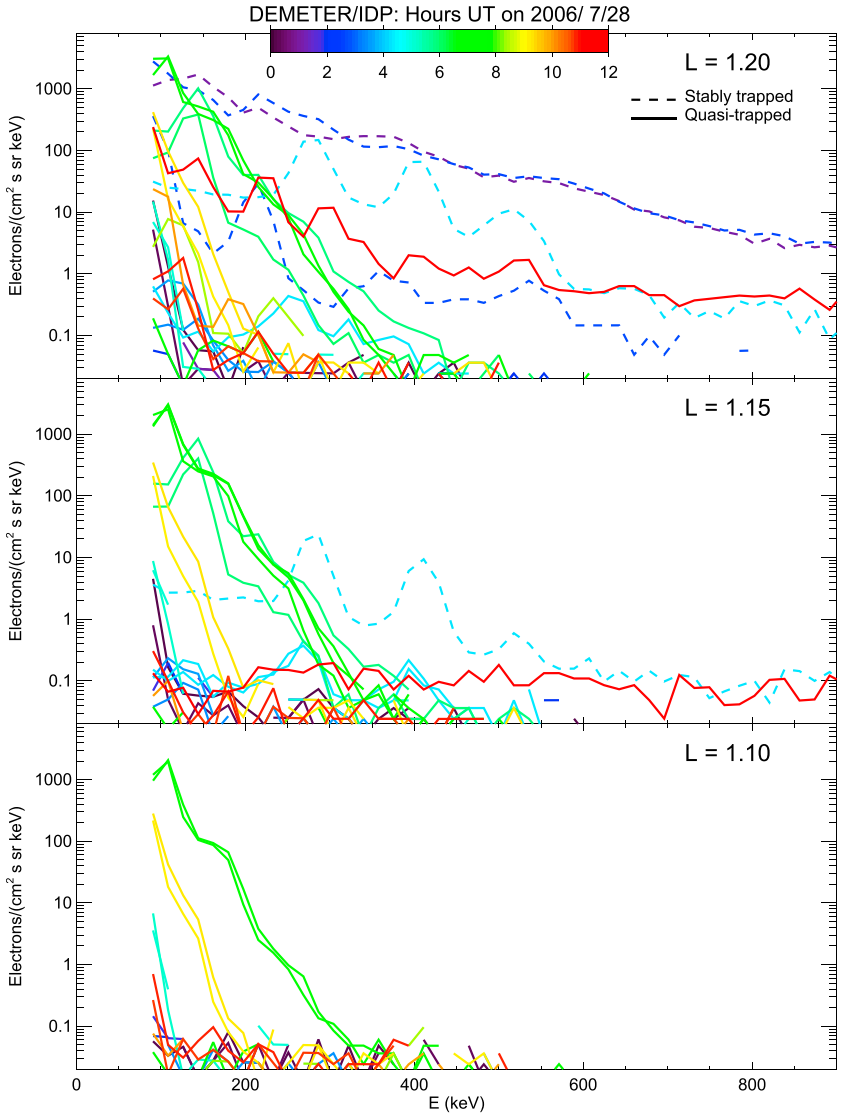

Figure 8. Similar to Figure 7 but for the B event period.

8. Possible Interpretations

Energetic electrons in the quasi-trapping region with $L < 1.15$ could not be scattered from stably trapped electrons at higher altitude because they would remain on the same magnetic field lines (within a gyroradius), and there is no such source population on those field lines. Then their likely origin is the stably trapped population at higher L, from where they must have been transported or injected. Here L is defined in the static IGRF-12 model, so this interpretation includes the possibility that drift shells were distorted by a time-dependent mechanism and are therefore mislabeled by L. Some ways this could happen are now considered.

First, drift shells are changed by a storm-time magnetic field, requiring a time-dependent external field model in addition to IGRF-12. A simple estimate of the resulting change in L is obtained by including a uniform southward magnetic field, opposing Earth's dipole field in the equatorial plane, of magnitude $|D_{st}|$. Conserving magnetic flux through the drift shell then produces the change (Selesnick & Kanekal, 2009) $\Delta L = |D_{st}|(LR_E)^3/(2k_0)$. Even with $D_{st} = -400$ nT (Figure 2), $\Delta L \sim 0.01$ at low L, which is too small to cause the observed injections.

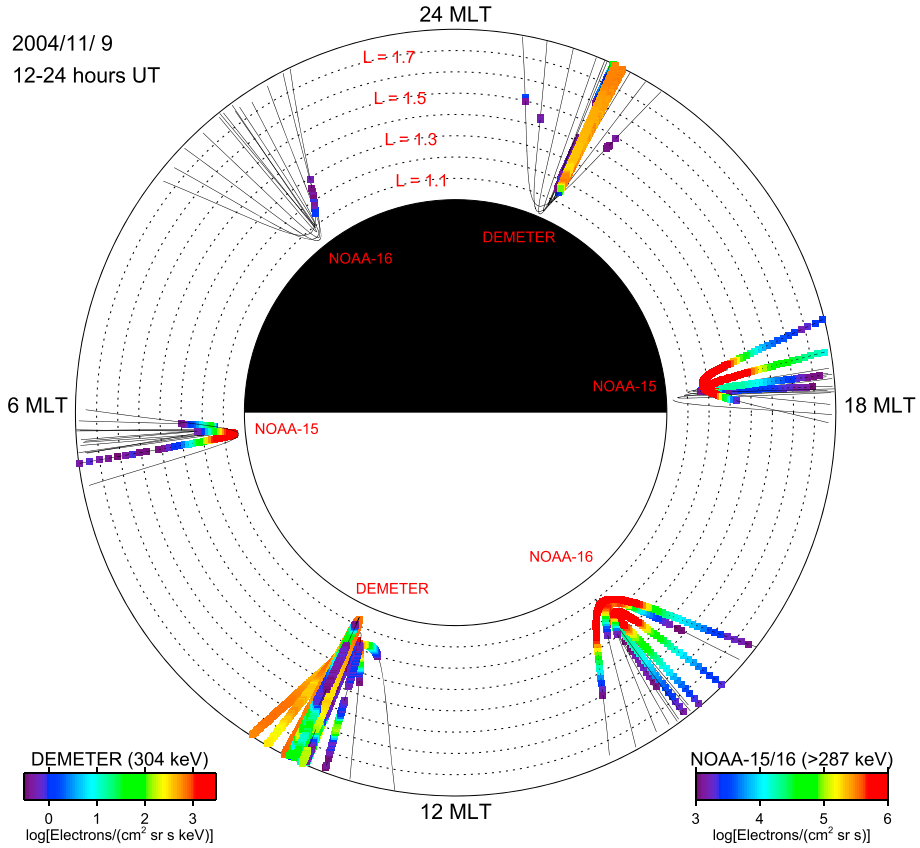

Figure 9. Orbital tracks from the A event period in polar L-MLT coordinates and color coded by measured electron intensity when it is above the lower intensity threshold. Concentric circles are separated by 0.1 in L. MLT = magnetic local time.

Next, the changing magnetic field also induces an electric field, which distorts existing drift shells. Assuming azimuthal symmetry, a rough estimate of the induced azimuthal electric field magnitude is $\mathcal{E}_{\text{ind}} = (\partial B/\partial t)LR_E/2$. Even with $\partial B/\partial t = 100$ nT/hr, $\mathcal{E}_{\text{ind}} \sim 0.1$ mV/m at low L which, as will be shown, is also too small to cause the observed injections.

Finally, drift shells could be further distorted by a changing large-scale quasi-static, or convection, electric field. If the change is slow compared to electron drift periods, then electrons will largely remain on the same drift shells as they distort. However, drift periods of ~100-keV electrons at low L are several hours, and changes this slow would be observed in progress over multiple satellite orbits. Therefore, it is more likely that the electric field changes more rapidly, in which case electrons would, in place, change their drift shells. Subsequent motion along their new drift paths could cause the injections that would be local time and energy dependent due to differing drift rates. Consequences of this idea are explored next.

9. Electron Injection Simulation

Sudden application of a uniform convection electric field causes electron drift shells to shift in the direction of the field. For example, a dawn-to-dusk electric field shifts the drift shells closer to Earth in the dawn sector and further away in the dusk sector (Selesnick et al., 2016). Electrons initially at dusk are then suddenly at lower L. Half a drift period later, they reach dawn on the new drift shell, which is now closer to Earth than the old one, forming the injection. Now they also have higher kinetic energy E and higher equatorial pitch angle α_0, due to conservation of the first two adiabatic invariants, and higher intensity $j = p^2 f$, due to conservation of phase space density f and their higher momentum p.

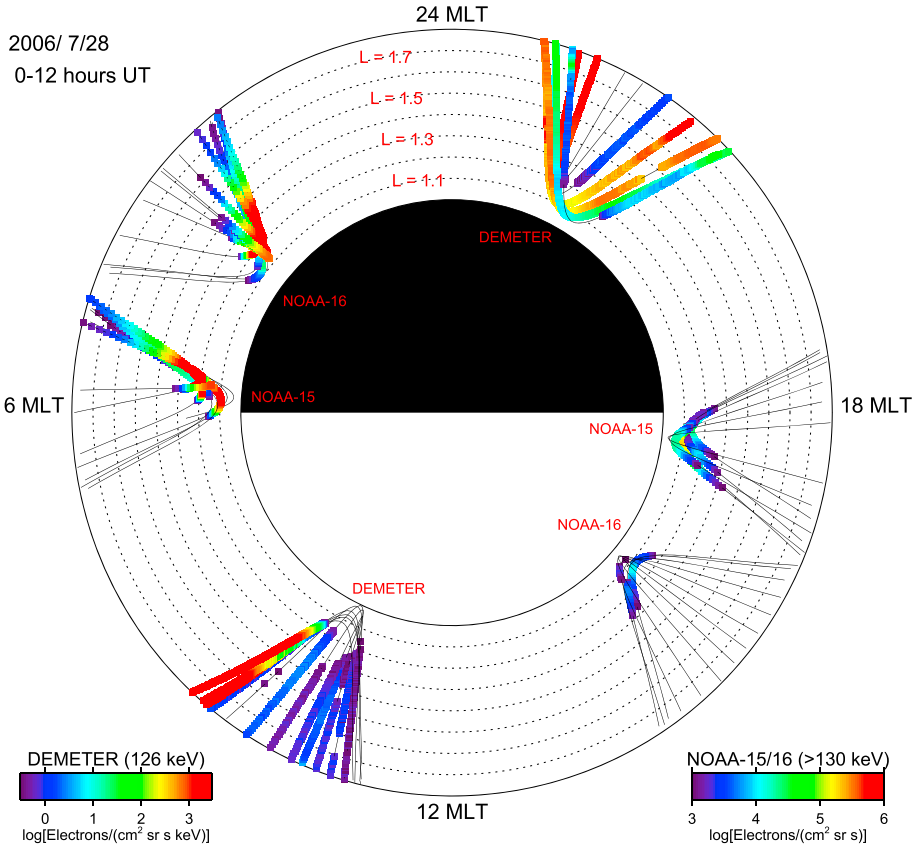

Figure 10. Similar to Figure 9 but for the B event period.

For a given electric field, first-order changes in L and E, assuming conservation of the first adiabatic invariant for equatorial electrons in a dipole magnetic field, are (Selesnick et al., 2016, with a slightly different notation)

$$\Delta L = \frac{eV_c L}{\frac{3}{2}\gamma mc^2\beta^2 - e(V_\Omega - V_c)}, \tag{1}$$

and

$$\Delta E = -\frac{3}{2}\gamma mc^2\beta^2\frac{\Delta L}{L}, \tag{2}$$

where the electrostatic potentials $V_c = \mathcal{E}_c L R_E \sin\phi$ for convection electric field magnitude $\mathcal{E}_c$ and $V_\Omega = -k_0\Omega/(cLR_E)$ for corotation frequency $\Omega = 7.3\times10^{-5}$ s^{-1}. The azimuth ϕ is based on the assumed direction of the convection electric field (for a dawn-to-dusk field $\phi = 0$ at midnight). Other symbols have their usual meaning (γ and β are the electron relativistic factors related to E, e is electron charge, and mc^2 is electron rest energy). Low-altitude satellite data require the formulae to be generalized to electrons mirroring off the equatorial plane, as is easily achieved assuming the second adiabatic invariant is also conserved, but resulting weak α_0 dependences and a small $\Delta\alpha_0$ are neglected here.

Simulation of an observed injection from a model radiation belt proceeds as follows: At the satellite location, L and E are changed to their updated values using (1) and (2) with an assumed constant electric field $\mathcal{E}_c$. Then the bounce-averaged electron drift rate at the α_0 value of the measurement, from a dipole approximation (Schulz & Lanzerotti, 1974, equation 1.35), is combined with corotational drift to determine the electron azimuth at the earlier time when the electric field was applied. Then L and E are changed again, back to their earlier values, by evaluating (1) and (2) at this earlier azimuth. Then the model inner belt intensity is evaluated, at the earlier L and E, and adjusted by the ratio of final to initial p^2. However, if the drift motion passed through the SAA longitude, assumed to be 0°, then the model intensity is set to zero. Finally, any required instrumental corrections are applied to the model intensity for comparison to observations.

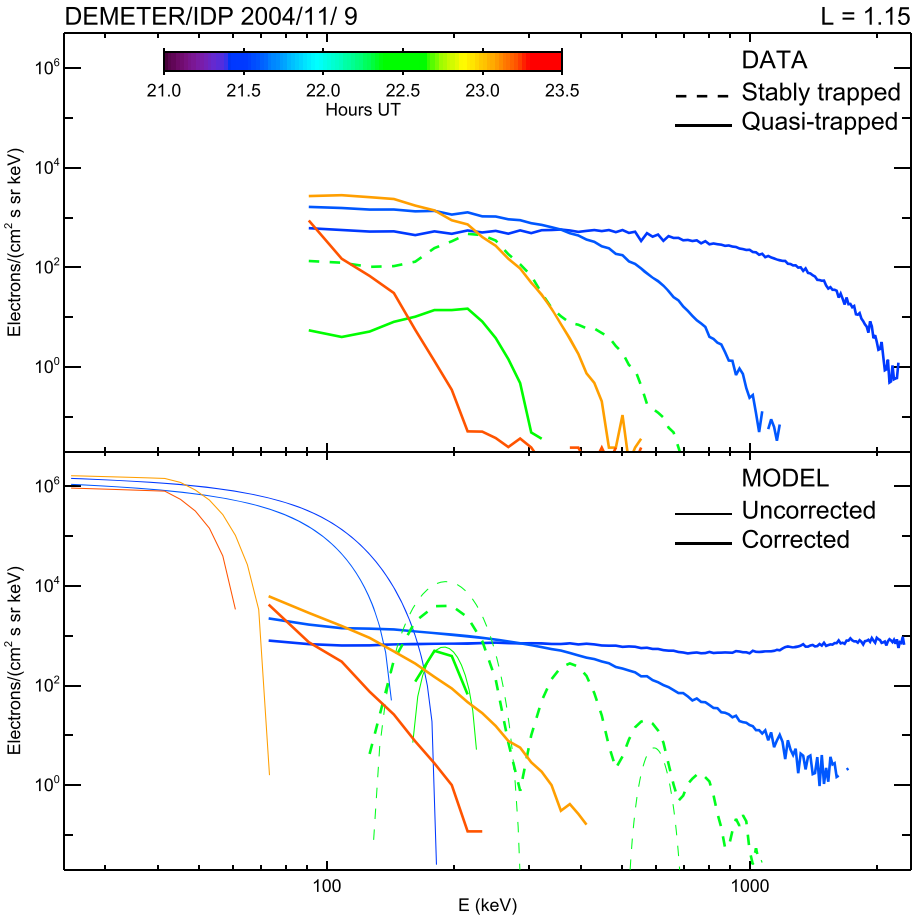

Figure 11. Measured (top) and simulated model (bottom) IDP energy spectra from event A at $L = 1.15$, color coded by UT. Uncorrected model spectra (thin lines) are also corrected (thick lines) to include instrumental deadtime and pileup for direct comparison to the data. Spectra are shown both from the quasi-trapping (solid) and stable trapping (dashed) regions.

Simulation results for IDP during event A, with the corresponding observations, are shown for $L = 1.15$ in Figure 11 and for $L = 1.1$ in Figure 12, including simulated electron energy spectra both without and with correction for instrument deadtime and pulse pileup (Appendix C). Uncorrected spectra (thin lines, now on a logarithmic energy scale) are the simulated values as they would be observed by a perfect detector; corrected spectra (thick lines) are adjusted to approximately account for these instrumental effects, for direct comparison to the IDP observations. The simulation is based on the quiet inner belt model (Appendix B) but using modified parameters for the active storm period: $j_0 = 2 \times 10^6$ (cm^2 s sr keV)$^{-1}$ and $n = 2.0$. The model electric field is 5 mV/m, oriented toward 4:00 MLT, and was turned on at 20:00 UT on 9 November.

In both figures, observed and corrected model electron spectra are in reasonable agreement, given the simplicity of the model. Electric field magnitude, direction, and turn-on time were chosen to achieve this (we do not attempt to model the later electric field turn-off with this simplified model). Initial model intensity is zero for $L \leq 1.15$, so all of the model intensities shown result from injection. Uncorrected model injected energy spectra are considerably softer than the quiet-time inner belt spectra because of strong energy dependence in ΔL, which decreases with increasing E. Injected spectra soften further with time as the higher energy electrons drift away from the satellite longitude.

Corrections to the model energy spectra are substantial in most cases. The model predicts that electrons apparently observed at kinetic energy up to ~2 MeV were, in fact, from pileup of high-intensity electrons with $E < 200$ keV and that intensity observed at low E was reduced by both pileup and deadtime. One measurement at $L = 1.15$ (solid green line in Figure 11) is unaffected by corrections, with a local maximum near 200 keV in both data and model. In another case, there are stably trapped electrons at $L = 1.15$ (dashed

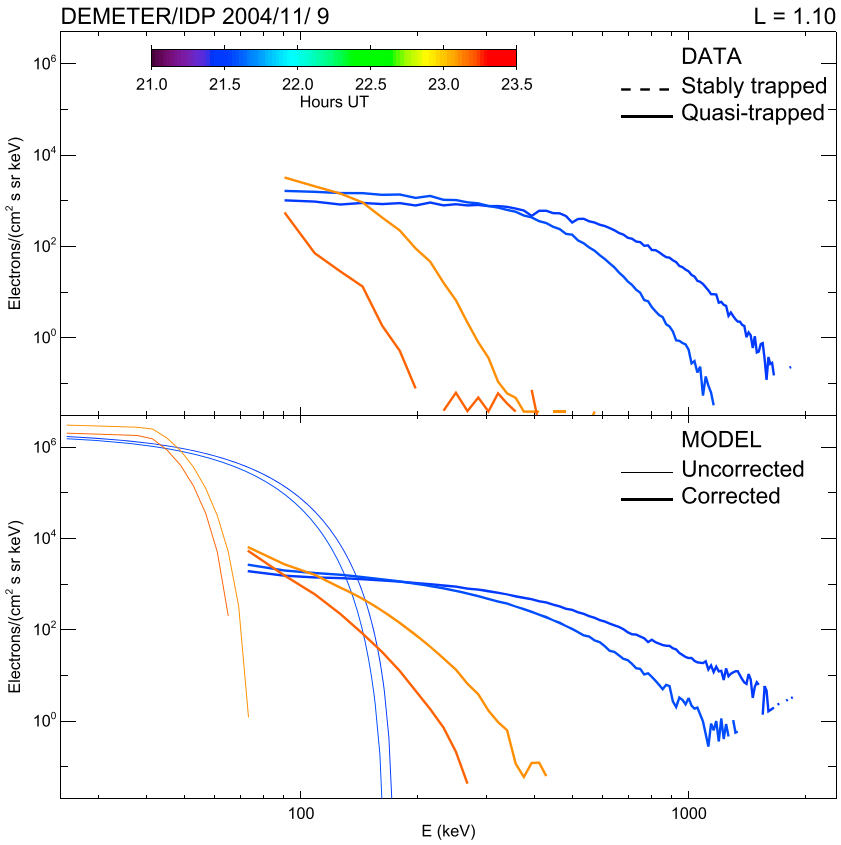

Figure 12. Similar to Figure 11 but for $L = 1.1$ where there is no stable trapping.

green line in Figure 11) that are not entirely modified, though the local maximum near 400 keV is a result of pileup from the true local maximum near 200 keV.

Simulated electron intensity versus L, from the same model for event A but now as observed by NOAA-16, are shown in Figure 13 with the data for comparison. Model differential intensity has been integrated above each energy threshold for comparison to measured integral intensity, without correction for pileup or deadtime as is appropriate in this case. High-intensity electrons were observed to low $L \approx 1.12$ during consecutive orbits. Their locations, not shown in the figure, were mostly outside the trapping region, near 100° E longitude and 14:00 MLT. Model predictions of injected electrons are in qualitative agreement with observations, and virtually none would be predicted without injection. Similar model results are obtained for NOAA-17 (data in Figure 5), near the same local time as DEMETER. However, for NOAA-15, which observed injected electrons to low L near 6:00 MLT (Figure 9) and 120° W longitude, the same model predicts no observation because the simulated injection did not reach that longitude, so data and model are inconsistent in that case.

10. Discussion and Conclusion

Energetic electrons of high intensity have been observed by IDP below the inner belt trapping region, at $L < 1.15$, on at least seven occasions over the DEMETER satellite lifetime (2004–2010), but all of these were during the more geomagnetically active interval before the end of 2006. The most intense such event, during the strong magnetic storm of November 2004, has been a primary subject of this study. The next most intense, on 15 May 2005 during another significant magnetic storm, was not studied here. Measurements have also been described here from a clear but less intense event on 28 July 2006, during a weak magnetic storm, because the data were less degraded by instrumental pileup and deadtime effects. Supporting data from the NOAA/POES satellites provide additional constraints on the differing magnitudes and local time dependences of each event.

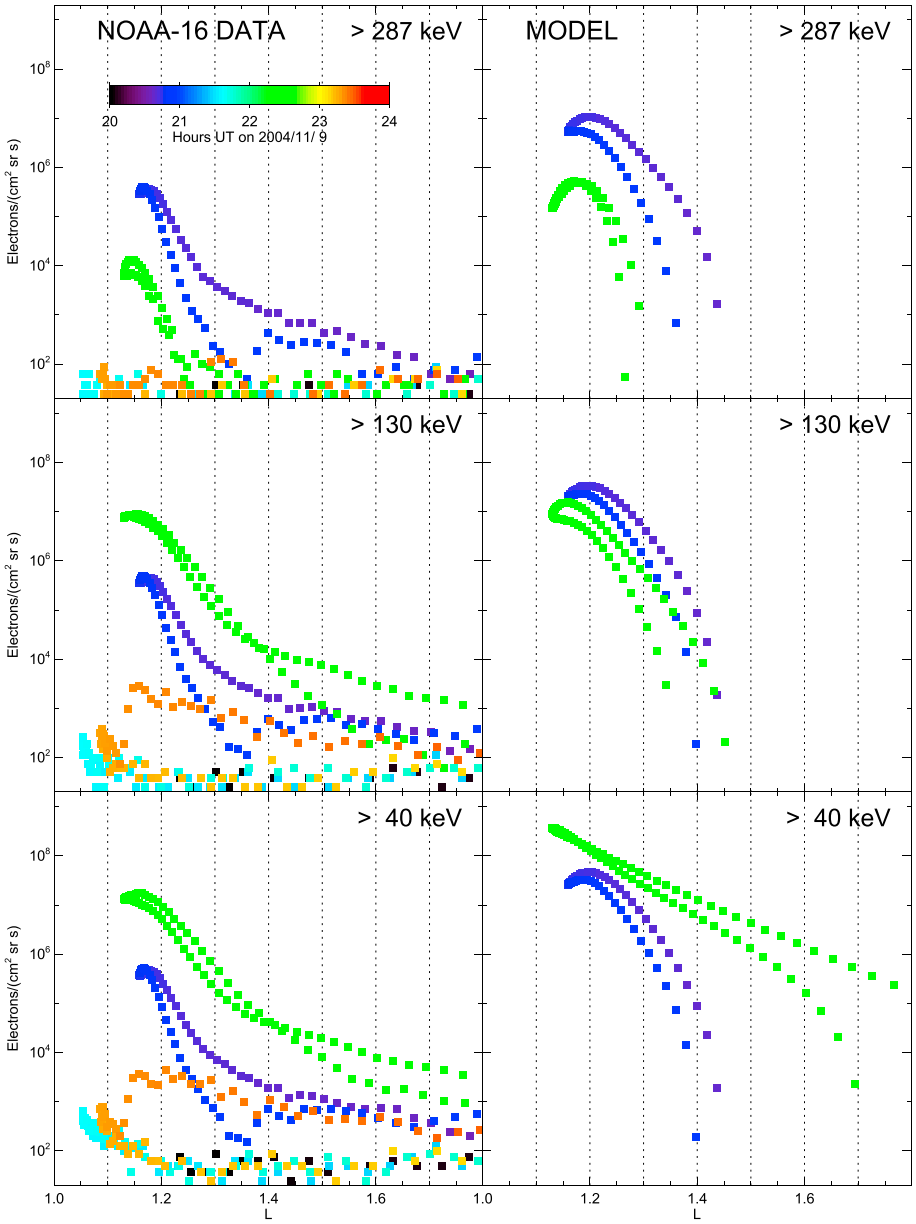

Figure 13. Measured (left) and simulated model (right) NOAA-16 electron integral intensity versus *L* for event A, color coded by UT.

The largest event is most useful for attempting to understand the cause of these electron injections, despite instrumental difficulties, because it is relatively isolated due to its size. Smaller events tend to be more complex because the lower edge of the inner belt itself usually has a complex structure during geomagnetically active times (resulting from drift echoes of earlier injections). Simulation of the November 2004 event shows that the injection can be caused by an enhanced convection electric field of magnitude ~5 mV/m, although the model cannot be optimized to accurately fit all of the data, which is unsurprising given its simplicity.

Electric fields at satellite altitude and at low *L* should correspond closely to the near-equatorial ionospheric electric field, after mapping along the magnetic field over distances of only a few hundred kilometers. Radar measurements from 9 November 2004 showed an eastward component of the dayside equatorial ionospheric electric field maximizing near 20:00 UT and 15:00 LT with magnitude ~2 mV/m, attributed to direct penetration of the interplanetary electric field to low latitudes (Huang, 2008). This maximum occurred at the same time as the inferred model electron injection that was observed ~1.2 hr later at low *L*. However,

the inferred ~5 mV/m was nearly in the opposite, westward dayside direction, as would be expected from an overshielding field (Kikuchi & Hashimoto, 2016), possibly combined with disturbance dynamo electric fields, following northward turning of the interplanetary magnetic field. A northward turning occurred near 21:00 UT. Clarification of these apparent inconsistencies will probably require comparison of the observations to electron test-particle simulations (Su et al., 2016) in a detailed low-latitude electric field model specific to the event under study (Hui & Vichare, 2019). Observed electron injections thus may provide a new means of testing current understanding of global electrodynamic processes. Such a test would, as a result of electron drift, be sensitive to remote electric fields and thereby complementary to local field measurements.

Appendix A: Possible Proton Response

Both the IDP and MEPED electron telescopes respond to energetic protons in addition to electrons. Accurate interpretation of each data set requires consideration of both possibilities within the observational context. For the data under study, a significant proton response is ruled out by the following arguments.

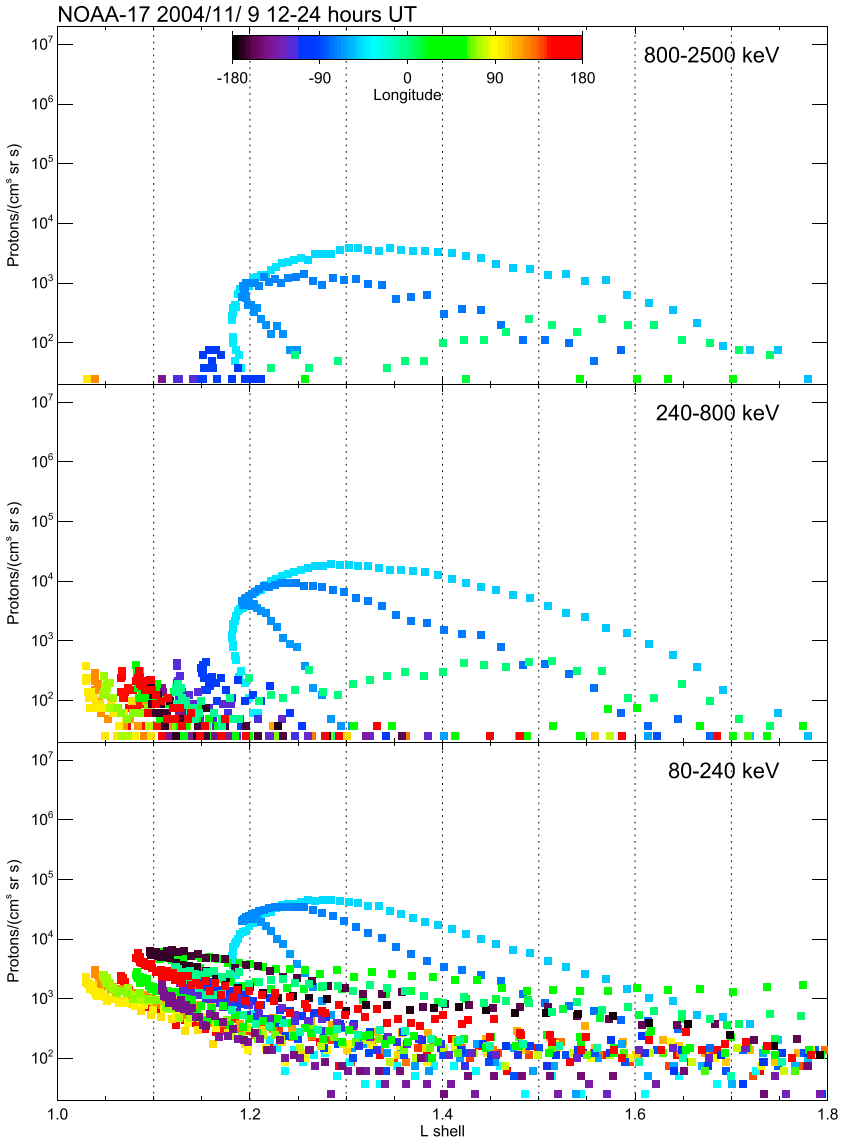

Figure A1. Measured intensity versus *L* from three NOAA-17/MEPED proton channels, for a 12-hr interval including the A event, color coded by geographic longitude.

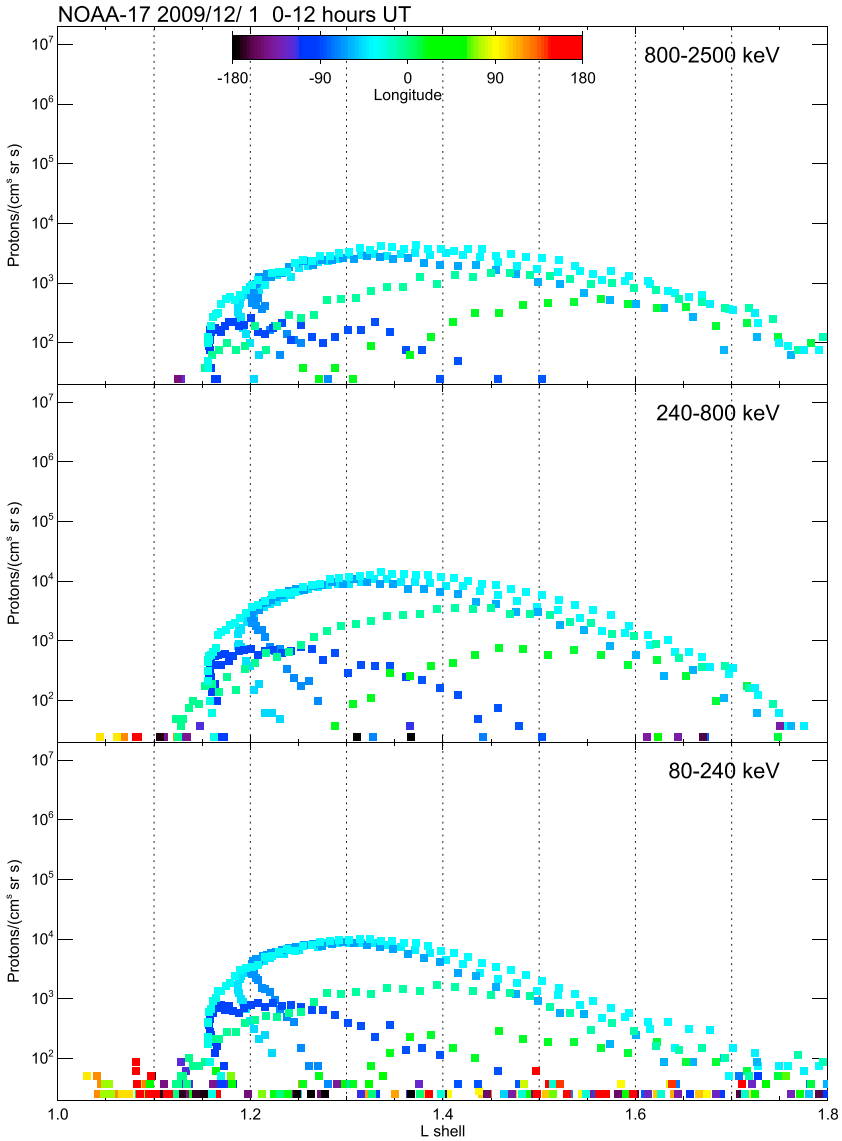

Figure A2. Similar to Figure A1 but from a 12-hr interval in 2009.

First, observations in the quasi-trapping region below $L = 1.15$, such as the A and B events in Figure 1, strongly favor the electron interpretation because of their geographic distribution. They are observed mostly, though not exclusively, closer to the west side of the SAA than to the east, consistent with possible formation at any longitude followed by eastward electron drift and eventual loss in the SAA. The opposite distribution would be expected for westward proton drift. This conclusion is supported by several other observed events, in addition to those shown in the figure.

If the low L events are electrons injected from the stably trapped inner belt, then there must be sufficient inner belt electron intensity to supply them. This supports an assumption that most of the SAA data taken concurrently are due to electrons rather than protons, consistent with the model simulations of section 9.

However, independent evidence is available that further supports an electron interpretation of the SAA data and thus also of the low L events. If the SAA data were due primarily to high-energy ($\gtrsim$10 MeV) radiation belt protons, then intensities should be relatively stable over time and slightly higher in 2009, due to solar minimum conditions, compared to 2004 or 2006 (Selesnick et al., 2007). That observed SAA intensity was significantly higher during 2004 and 2006 (Figure 1) shows that this was not true. The reduction in SAA electron intensity observed by DEMETER/IDP from 2006 to 2009 is confirmed by POES data. It is likely that

the 2009 SAA data are primarily from high-energy protons, but even at the same level, they would not have made a significant contribution to the inner belt response in 2004 or 2006.

The IDP response also includes lower energy protons that stop in the detector after passing through the Al foil window. Their possible incident energies are ~580–2,600 keV, corresponding to the ~70–2,400 keV range of the electron channels. A response in the SAA to protons of these energies can be ruled out in favor of electrons with help from POES/MEPED data.

The MEPED electron telescope has some response to protons, while the MEPED proton telescope has some response to electrons (Yando et al., 2011). Proton telescope data from 9 November 2004, in the nominal energy range 80–2,500 keV, are shown versus L in Figure A1, for comparison to the electron telescope data in Figure 5. In the SAA (blue and green points), electron telescope intensity is considerably higher than proton telescope intensity. This shows that the electron telescope response is primarily to electrons rather than protons; otherwise, they would also be seen by the proton telescope.

Proton telescope response outside the SAA at low L (Figure A1) is difficult to interpret but may be indicative of low-energy proton injection from the stably trapped population. A similar response was also seen in the electron telescope (Figure 5). Proton telescope data from 1 December 2009 are shown in Figure A2. The SAA intensities are similar to the earlier data, confirming that they are due to protons, probably of high energy. In 2009, there was little response outside the SAA, unlike in 2004, when it must have been related to the geomagnetically active conditions.

Appendix B: Quiet Inner Belt Model

The quiet-time inner belt electron intensity model is a fit to IDP data taken prior to the November 2004 magnetic storm. As a function of E, L, and $x = \cos\alpha_0$, it is

$$j(E,L,x) = j_0 \exp\left(\frac{-E}{E_0}\right)\left(1 - \exp\left[\frac{L_1 - L}{0.15}\right]^4\right)\left(1 - \left[\frac{x}{x_c}\right]^2\right)^n, \tag{B1}$$

where α_0 is equatorial pitch angle, x_c is the equatorial pitch angle cosine at the stable trapping boundary, defined by $x_c^2 = 1 - B_0/B'_{100}$, equatorial field magnitude is B_0, and the constants $j_0 = 5 \times 10^5$ (cm^2 s sr keV)$^{-1}$, $E_0 = 120$ keV, $n = 1.5$, and $L_1 = 1.15$. It is defined only for the stable trapping region $x > x_c$ and for $L > L_1$.

Model electron intensity at selected IDP energies for DEMETER orbital passes through the SAA region on 6 November 2004, with x determined by the IDP orientation, is shown versus L in Figure B1, both uncorrected and corrected for pileup and deadtime (Appendix C). Observed values, also shown, are in reasonable agreement, though the model simplicity precludes an accurate fit.

Appendix C: IDP Pileup and Deadtime Corrections

Laboratory testing of IDP electronics under high counting-rate conditions is unavailable, and estimates described here are based on simplified pileup and deadtime models constrained by orbital data. The goal is to adjust, or correct, a known model electron intensity j to include effects of pileup and deadtime for direct comparison to IDP data. (An inverse correction that would adjust data for comparison to the unmodified j is impractical.)

First, j is converted to an energy distribution of counting rate in the detector, after passing through the 6-μm Al foil window, $r^{\mathrm{det}}(E') = j(E)G(E)S(E)/S(E')$, where E' is the electron energy reaching the detector that corresponds to energy E outside the telescope, G is the energy dependent IDP geometry factor (Sauvaud et al., 2006, Figure 7), and $S = -dE/dx$ is the Al foil stopping power for thickness x (Berger et al., 2017). (A minimum energy of $E = 24$ keV is required to reach the detector, with $E' = 0$.) Then, time gaps between electron arrivals are determined by Monte Carlo simulation of exponential waiting times based on the total rate of all electrons reaching the detector, $R^{\mathrm{det}} = \int r^{\mathrm{det}}(E')dE'$. For pileup, it is assumed that all electron pulses arriving without any time gap longer than τ_s, the amplifier shaping time, add to form a single, larger pulse. When a longer gap occurs, then a new addition begins. Individual pulse heights are generated by random sampling from the distribution $r^{\mathrm{det}}(E')$. After pulses pile up to higher energy, they are accumulated to form a modified rate distribution $r^{\mathrm{pu}}(E')$.

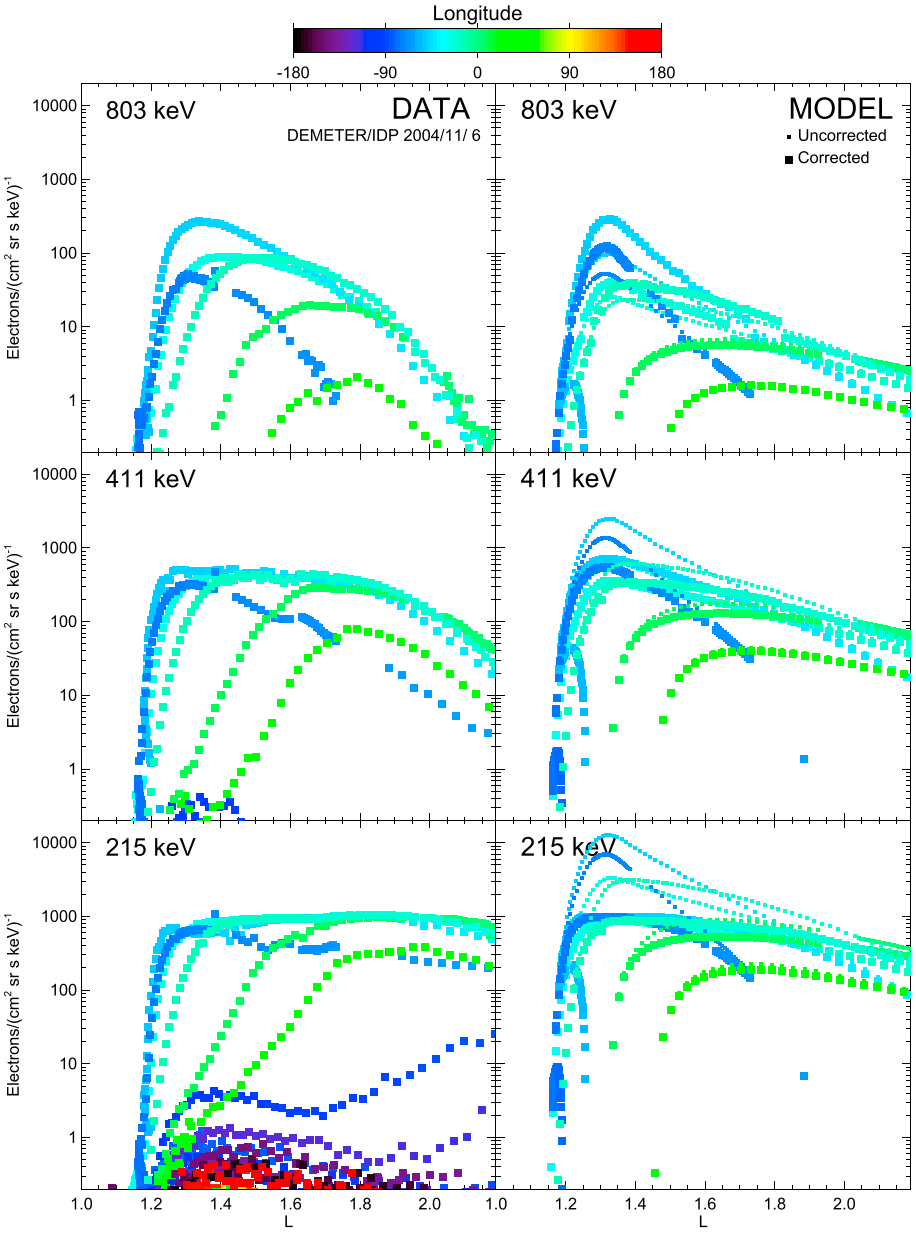

Figure B1. (left) Intensity versus L measured by IDP at three selected energies on 6 November 2004, color coded by geographic longitude. (right) Corresponding model intensity without (small symbols) and with (large symbols) correction for pileup and deadtime.

Next, the modified rate distribution is binned into energy channels of width $\Delta E = 17.8$ keV, beginning at $E' = 64$ keV, above which the difference between E and E' is negligible. Now $r_i^{\rm pu}$ is the piled-up rate for channel i with mean energy E_i.

However, not all pulses can be counted due to deadtime, for which a further correction is needed. If every pulse produced the same deadtime τ, then the corrected average time gap between counts would be longer by that amount, $1/r_i^{\rm cor} = 1/r_i^{\rm pu} + \tau$, where $r_i^{\rm cor}$ is the corrected rate for channel i. But deadtime typically depends on both the previous energy deposit that caused it, say in channel j, and on the energy deposit to be measured in channel i. Then the time between counts requires an average deadtime weighted by the ratio of rates at the previous and measured energies, $1/r_i^{\rm cor} = 1/r_j^{\rm pu} + \sum_j \tau_{ij} r_j^{\rm pu}/r_i^{\rm pu}$, where τ_{ij} is a deadtime matrix. Dependence on the previous energy is typically weaker and is neglected here for simplicity, so the deadtime $\tau_{ij} = \tau_i$, depending only on E_i, and the average deadtime for channel i is $\tau_i R_{\rm pu}/r_i^{\rm pu}$, where $R_{\rm pu} = \sum_j r_j^{\rm pu}$ is the

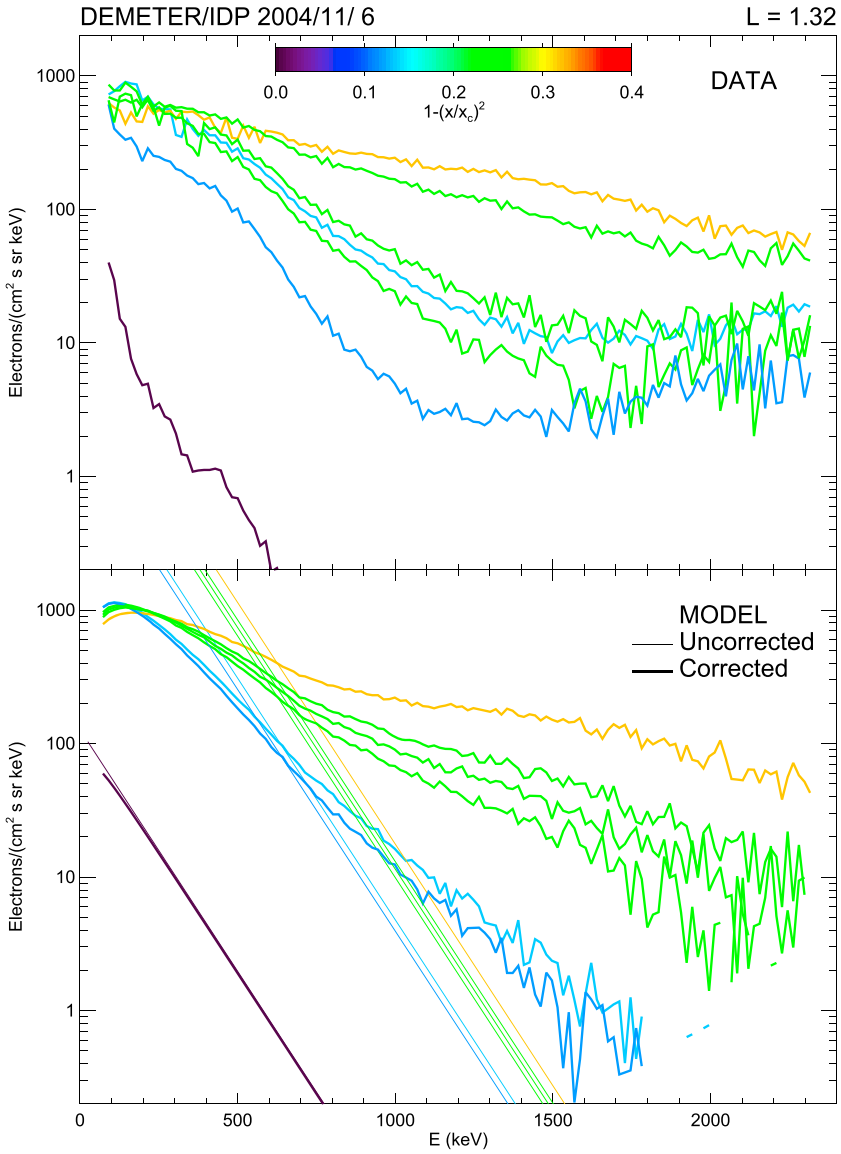

Figure C1. (top) Energy spectra measured by IDP at $L = 1.32$ on 6 November 2004, color coded by a quantity that increases into the stable trapping region (as defined in B). (bottom) Corresponding model spectra without (thin lines) and with (thick lines) correction for instrumental pileup and deadtime.

total uncorrected rate after pileup. Finally, the corrected rate is $r_i^{\rm cor} = r_i^{\rm pu}/(1 + \tau_i R_{\rm pu})$, which is converted to corrected model intensity, $j_i^{\rm cor} = r_i^{\rm cor}/[G(E_i)\Delta E]$.

A shaping time of $\tau_s = 200$ ns and a deadtime of $\tau_i = (400\ \mu\text{s keV})/E_i$ were found to give reasonable agreement with observations, as shown in Figure C1. The model distribution j is from the quiet-time inner belt model (Appendix B) for each satellite crossing of $L = 1.32$ on 6 November 2004, providing a range of electron intensities. Uncorrected and corrected model energy spectra are shown, as are measured energy spectra, color coded by $1 - (x/x_c)^2$ (defined in Appendix B). As intensity increases, the corrected spectra are seen to harden due to pileup and to saturate at low energy due to deadtime, in qualitative agreement with the corresponding measured spectra. The energy dependence of the deadtime was chosen so that only lower channels saturate, as observed (see also Figure 3). Due to the simplifying assumption of a square pulse shape, the derived amplifier shaping time is expected to be somewhat shorter than the actual value. Some measured spectra show increasing intensity at high energy that is probably due to high-energy proton response, not

included in the model, combined with decreasing G. Also, measurements are not perfectly ordered by x, as assumed in the simplified inner belt model.

Acknowledgments
We thank C.-S. Huang, J. M. Albert, and X. Li for helpful discussions. DEMETER data, NOAA satellite data, and geomagnetic indices are available online (https://cdpp-archive.cnes.fr/, https://satdat.ngdc.noaa.gov/, and http://wdc.kugi.kyoto-u.ac.jp/, respectively). This work was supported by the Space Vehicles Directorate of the Air Force Research Laboratory.

References

Albert, J. M., Starks, M. J., Horne, R. B., Meredith, N. P., & Glauert, S. A. (2016). Quasi-linear simulations of inner radiation belt electron pitch angle and energy distributions. *Geophysical Research Letters*, *43*, 2381–2388. https://doi.org/10.1002/2016GL067938

Berger, M. J., Coursey, J. S., Zucker, M. A., & Chang, J. (2017). Stopping-power and range tables for electrons, protons, and helium ions. Gaithersburg, MD: NIST, Physical Measurement Laboratory. https://doi.org/10.18434/T4NC7P

Evans, D. S., & Greer, M. S. (2000). Polar orbiting environmental satellite space environmental monitor-2: Instrument descriptions and archive data documentation. Boulder, CO: Natl. Atmos. and Oceanic Admin., Space Environ. Cent.

Huang, C.-S. (2008). Continuous penetration of the interplanetary electric field to the equatorial ionosphere over eight hours during intense geomagnetic storms. *Journal of Geophysical Research*, *113*, A11305. https://doi.org/10.1029/2008JA013588

Hui, D., & Vichare, G. (2019). Variable responses of equatorial ionosphere during undershielding and overshielding conditions. *Journal of Geophysical Research: Space Physics*, *124*, 1328–1342. https://doi.org/10.1029/2018JA025999

Kikuchi, T., & Hashimoto, K. K. (2016). Transmission of the electric fields to the low latitude ionosphere in the magnetosphere-ionosphere current circuit. *Geoscience Letters*, *3*, 4. https://doi.org/10.1186/s40562-016-0035-6

Roederer, J. G. (1970). *Dynamics of geomagnetically trapped radiation*. Berlin: Springer.

Sauvaud, J. A., Moreau, T., Maggiolo, R., Treilhou, J. P., Jacquey, C., Cros, A., et al. (2006). High-energy electron detection onboard DEMETER: The IDP spectrometer, description and first results on the inner belt. *Planetary and Space Science*, *54*, 502–511. https://doi.org/10.1016/j.pss.2005.10.019

Schulz, M., & Lanzerotti, L. J. (1974). *Particle diffusion in the radiation belts*. Berlin: Springer.

Selesnick, R. S. (2012). Atmospheric scattering and decay of inner radiation belt electrons. *Journal of Geophysical Research*, *117*, A08218. https://doi.org/10.1029/2012JA017793

Selesnick, R. S. (2015). Measurement of inner radiation belt electrons with kinetic energy above 1 MeV. *Journal of Geophysical Research: Space Physics*, *120*, 8339–8349. https://doi.org/10.1002/2015JA021387

Selesnick, R. S. (2016). Stochastic simulation of inner radiation belt electron decay by atmospheric scattering. *Journal of Geophysical Research: Space Physics*, *121*, 1249–1262. https://doi.org/10.1002/2015JA022180

Selesnick, R. S., Albert, J. M., & Starks, M. J. (2013). Influence of a ground-based VLF radio transmitter on the inner electron radiation belt. *Journal of Geophysical Research: Space Physics*, *118*, 628–635. https://doi.org/10.1002/jgra.50095

Selesnick, R. S., & Kanekal, S. G. (2009). Variability of the total radiation belt electron content. *Journal of Geophysical Research*, *114*, A02203. https://doi.org/10.1029/2008JA013432

Selesnick, R. S., Looper, M. D., & Mewaldt, R. A. (2007). A theoretical model of the inner proton radiation belt. *Space Weather*, *5*, S04003. https://doi.org/10.1029/2006SW000275

Selesnick, R. S., Su, Y.-J., & Blake, J. B. (2016). Control of the innermost electron radiation belt by large-scale electric fields. *Journal of Geophysical Research: Space Physics*, *121*, 8417–8427. https://doi.org/10.1002/2016JA022973

Su, Y.-J., Selesnick, R. S., & Blake, J. B. (2016). Formation of the inner electron radiation belt by enhanced large-scale electric fields. *Journal of Geophysical Research: Space Physics*, *121*, 8508–8522. https://doi.org/10.1002/2016JA022881

Suvorova, A. V. (2017). Flux enhancements of >30 keV electrons at low drift shells $L < 1.2$ during last solar cycles. *Journal of Geophysical Research: Space Physics*, *122*, 12,274–12,287. https://doi.org/10.1002/2017JA024556

Suvorova, A. V., Huang, C. M., Matsumoto, H., Dmitriev, A. V., Kunitsyn, V. E., Andreeva, E. S., et al. (2014). Low-latitude ionospheric effects of energetic electrons during a recurrent magnetic storm. *Journal of Geophysical Research: Space Physics*, *119*, 9283–9302. https://doi.org/10.1002/2014JA020349

Thébault, E., Finlay, C. C., Beggan, C. D., Alken, P., Aubert, J., Barrois, O., et al. (2015). International geomagnetic reference field: The 12th generation. *Earth, Planets, and Space*, *67*, 79. https://doi.org/10.1186/s40623-015-0228-9

Yando, K., Millan, R. M., Green, J. C., & Evans, D. S. (2011). A Monte Carlo simulation of the NOAA POES Medium Energy Proton and Electron Detector instrument. *Journal of Geophysical Research*, *116*, A10231. https://doi.org/10.1029/2011JA016671

Zhang, K., Li, X., Zhao, H., Schiller, Q., Khoo, L. Y., Xiang, Z., et al. (2019). Cosmic Ray Albedo Neutron Decay (CRAND) as a source of inner belt electrons: Energy spectrum study. *Geophysical Research Letters*, *46*, 544–552. https://doi.org/10.1029/2018GL080887